Available online at www.sciencedirect.com
SCIENCE DIRECT
Physica D 217 (2006) 88–101
PHYSICA D
www.elsevier.com/locate/physd

Chaotic dynamics of the elliptical stadium billiard in the full parameter space

V. Lopac[a,*], I. Mrkonjić[b], N. Pavin[b], D. Radić[b]

[a] *Department of Physics, Faculty of Chemical Engineering and Technology, University of Zagreb, HR 10000 Zagreb, Croatia*
[b] *Department of Physics, Faculty of Science, University of Zagreb, HR 10000 Zagreb, Croatia*

Received 2 September 2005; received in revised form 21 February 2006; accepted 24 March 2006

Communicated by J. Stark

Abstract

Dynamical properties of the elliptical stadium billiard, which is a generalization of the stadium billiard and a special case of the recently introduced mushroom billiards, are investigated analytically and numerically. In its dependence on two shape parameters δ and γ, this system reveals a rich interplay of integrable, mixed and fully chaotic behavior. Poincaré sections, the box counting method and the stability analysis determine the structure of the parameter space and the borders between regions with different behavior. Results confirm the existence of a large fully chaotic region surrounding the straight line $\delta = 1 - \gamma$ corresponding to the Bunimovich circular stadium billiard. Bifurcations due to the hour-glass and multidiamond orbits are described. For the quantal elliptical stadium billiard, statistical properties of the level spacing fluctuations are examined and compared with classical results.

Keywords: Chaos; Billiard; Orbit stability; Energy level fluctuations; Elliptical stadium

1. Introduction

An elliptical stadium is a two-parameter planar domain constructed by adding symmetrically two half-ellipses to the opposite sides of a rectangle. In the corresponding elliptical stadium billiard, the point particle is moving with constant velocity within this boundary, exhibiting specular reflections on the walls. This billiard is a generalization of the Bunimovich stadium billiard with circular arcs [1], which is fully ergodic for any length of the central rectangle. When the semicircles are replaced by half-ellipses, a plethora of new dynamical properties emerges, ranging from exact integrability, through mixed dynamics with a single chaotic component or with a finely fragmented phase space, to broad regions of fully developed chaos. Thanks to these properties the elliptical stadium billiard can be considered a paradigmatic example of a Hamiltonian dynamical system, which convincingly illustrates both gradual and abrupt transitions induced by the parameter variation.

To appreciate these advantages, the system should be looked at as a whole. Several descriptions of the elliptical stadium billiard can be found in the literature [2–7]. However, although detailed and mathematically rigorous, they concentrate on some specific billiard properties and consider only restricted parameter regions. Therefore in the present analysis we take into account all possible boundary shapes and investigate the properties of the elliptical stadium billiard in the full parameter space spanned by two variables δ and γ. Some of the preliminary results for special cases with the present parametrization were described in [8] and [9]. The elliptical stadium billiard can also be considered as a special case of the recently introduced mushroom billiards [10,11].

Our interest for the elliptical stadium billiard has been enhanced by a number of recent experiments and applications. Dynamical properties of classical and quantal billiards have important consequences for realistic systems in optics as well as in atomic, mesoscopic and solid state physics. Here we quote only a few examples. Details of the classical and quantal billiard dynamics are the necessary tools for designing properties of semiconducting microlasers and optical devices used in communication technologies [12,13]. Measured conductance fluctuations in the semiconductor quantum dots

* Corresponding address: Department of Physics, Faculty of Chemical Engineering and Technology, University of Zagreb, Marulicev trg 19, HR 10000 Zagreb, Croatia. Tel.: +385 1 45 97 106; fax: +385 1 45 97 135.
E-mail address: vlopac@marie.fkit.hr (V. Lopac).

0167-2789/$ - see front matter © 2006 Published by Elsevier B.V.
doi:10.1016/j.physd.2006.03.014

of different shapes are obtained from the wave functions of the corresponding quantal billiards [14,15]. The "atom-optics" billiards formed by laser beams allow ultracold atoms to move within confined regions of desired shape [16–18]. In the nonimaging optics, the billiard properties determine the shapes of the absolutely focusing mirrors [19]. As a consequence of the recent technological interest in nanowires and similar extended microstructures, different problems with the open billiards have also been investigated [20,21], including the mushroom billiards [22]. Experiments performed with the stadium-shaped microwave resonant cavities [23,24] could be easily extended to stadia with elliptical arcs, predictably with interesting results.

In Section 2 we define the billiard boundary and describe its geometrical properties. In Section 3 the classical dynamics of the elliptical stadium billiard is presented. The existence and stability of some selected orbits are investigated by means of the Poincaré plots and orbit diagrams. Properties of the elliptic islands, their evolution and the bifurcations induced by the variation of the shape parameters are presented. The extent and limits of regions in the parameter space with different dynamical behavior are shown. In Section 4 further analysis of the Poincaré sections is presented. The extent of the chaotic region of the phase space is numerically estimated by means of the box-counting method. In Section 5 we consider the quantum-mechanical version of the elliptical stadium billiard, present selected results for the level spacing statistics, and compare them with the classical results for the chaotic fraction of the phase space. Finally, in Section 6 we discuss the obtained results and propose further investigations.

2. Geometrical properties of the elliptical stadium

The elliptical stadium is a closed planar domain, whose boundary in the x–y plane is defined by means of two parameters δ and γ, satisfying the conditions $0 \le \delta \le 1$ and $0 < \gamma < \infty$. It is symmetrical with respect to the x- and y-axis and is described in our parametrization as

$$y(x) = \begin{cases} \pm\gamma & \text{if } 0 \le |x| < \delta \\ \pm\gamma\sqrt{1 - \left(\dfrac{|x| - \delta}{1 - \delta}\right)^2} & \text{if } \delta \le |x| \le 1. \end{cases} \tag{1}$$

The meaning of parameters is visible from Fig. 1(a). The horizontal diameter is normalized to 2. The vertical semiaxis of the ellipse is γ, and the height 2γ of the billiard extends from 0 to ∞. The horizontal length of the central rectangle is 2δ, and the horizontal semiaxis of the ellipse is $1 - \delta$.

The limiting boundary subclasses for some specific parameter combinations are as follows. For $\delta = 0$ the shape is elliptical, for $\delta = 1$ it is rectangular. Especially, for $\delta = \gamma = 1$ it is a square, and for $\delta = 0$ and $\gamma = 1$ a circle. For $\delta = 1 - \gamma$ one obtains the Bunimovich stadia [1] with different lengths of the central rectangle, which define the border separating two distinct boundary classes, one for $\delta < 1 - \gamma$ with elongated semiellipses, and the other with $\delta > 1 - \gamma$ and flattened semiellipses. Another interesting case is $\delta = \gamma$, where the central rectangle is a square, and whose properties were briefly discussed in [8].

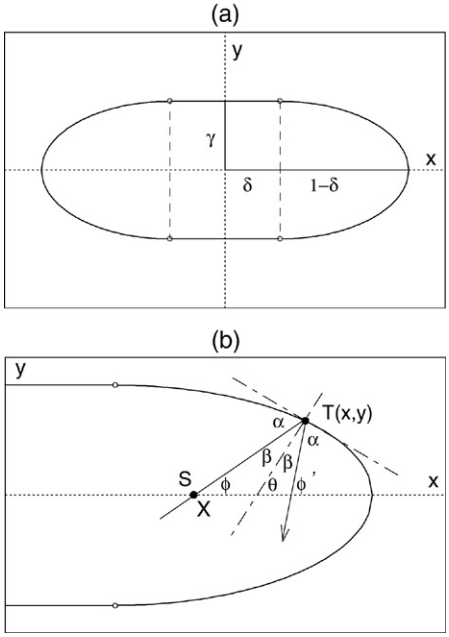

Fig. 1. (a) Shape parameters δ and γ for the elliptical stadium. (b) Meaning of the angles ϕ, ϕ', θ, α and β.

The focal points differ for the two classes. For $\delta > 1 - \gamma$ there are four foci at the points

$$F\left[\pm\delta, \pm\sqrt{\gamma^2 - (1 - \delta)^2}\right], \tag{2}$$

and for $\delta < 1 - \gamma$ the two foci are situated at the points

$$F\left[\pm\left(\delta + \sqrt{(1 - \delta)^2 - \gamma^2}\right), 0\right]. \tag{3}$$

These expressions enhance the importance of the term $\tau = \gamma^2 - (1 - \delta)^2$ which is negative for $\delta < 1 - \gamma$, positive for $\delta > 1 - \gamma$, and zero for $\delta = 1 - \gamma$ (Bunimovich stadium). For $\delta \le |x| \le 1$, the curvature radius is

$$R = \frac{[(1 - \delta)^4 + (|x| - \delta)^2[\gamma^2 - (1 - \delta)^2]]^{3/2}}{\gamma(1 - \delta)^4}. \tag{4}$$

For $0 \le |x| < \delta$ the boundary is flat and the curvature radius is $R = \infty$. At the endpoints of the horizontal and the vertical axis of the ellipse the curvature radius is $R_1 = \gamma^2/(1 - \delta)$ and $R_\delta = (1 - \delta)^2/\gamma$, respectively. It is $R = 1 - \delta$ for the circular arcs of the Bunimovich stadium. Fig. 2 shows some typical shapes of the elliptical stadia for δ between 0 and 1 and for γ between 0.25 and 1.5. The parameter γ can have any value between zero and infinity. However, at $\gamma = 0$ the boundary degenerates into a line, and the values of γ greater than 1.5 do not introduce any essentially new features.

3. Classical dynamics of the elliptical stadium billiard

Dynamics of a classical planar billiard can be examined by calculating the points on the billiard boundary where impacts and elastic reflections of the particle take place. Fig. 1(b) shows the meaning of variables describing an impact and appearing in

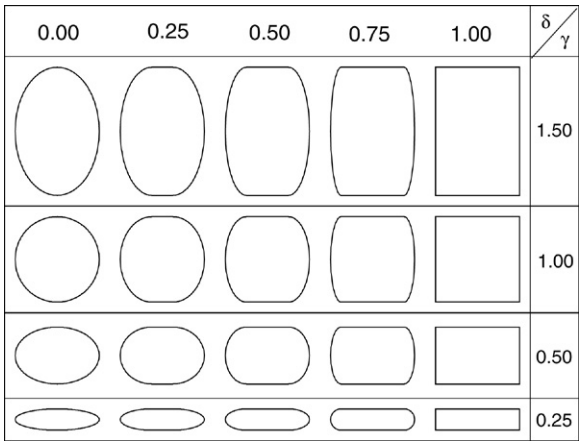

Fig. 2. Shapes of the elliptical stadium in dependence on δ and γ. Two of them ($\delta = \gamma = 0.50$ and $\delta = 0.75$, $\gamma = 0.25$) are Bunimovich stadia.

the conditions for existence and stability of orbits. Symbols ϕ and ϕ', respectively, denote the angles which the directions of the incoming and the outcoming path make with the x-axis. The normal to the boundary at the impact point T closes the angle $\theta = (\phi + \phi')/2$ with the x-axis. The angle between the normal and the incoming (or outcoming) path is $\beta = (\phi' - \phi)/2$, and $\alpha = (\pi/2) - \beta$ is the angle between the tangent to the boundary at the impact point T(x, y) and the incoming (or outcoming) path. The slope of the normal to the boundary at the impact point is given as the negative inverse derivative $\tan\theta = -1/y'$. For the iterative numerical computation of the impact points it is useful to know the relation between the slopes of the incident and the outgoing path, expressed as

$$\frac{2\tan\theta}{1-\tan^2\theta} = \frac{\tan\phi + \tan\phi'}{1 - \tan\phi\tan\phi'}. \tag{5}$$

In our numerical computations, two separate sets of data were obtained: coordinates x, y of the impact points on the billiard boundary, needed for the graphical presentation of the orbits and for the computations of the orbit stability, and coordinates X and V_x, suitable for the graphical presentation of the Poincaré sections. The points P(X, V_x) in the Poincaré diagrams are obtained by plotting as X the x-coordinate of the point S in which the rectilinear path segment crosses the x-axis, and as $V_x = \cos\phi$ the projection of the velocity on the x-axis. With an additional assumption concerning the horizontal diametral orbit (explained in Section 3.2) the Poincaré sections are thus completely defined. As some orbit segments do not cross the x-axis, the number of points in the Poincaré diagram can be smaller than the number of the impact points on the boundary. In our chosen system of units the mass and the velocity of the particle are $m = 1$ and $V = 1$, respectively, hence both X and V_x lie in the interval $[-1, 1]$. For billiards with noncircular boundary segments [8,25] such variables are computationally more convenient than those containing the arc length variable suitable for the billiard boundaries with circular arcs [26]. Since X and V_x are canonically conjugated variables and our billiard is a Hamiltonian system which reduces to the collision-to-collision symplectic twist map, the phase space and the corresponding Poincaré sections are area preserving.

Depending on the choice of the shape parameters and on initial conditions, one obtains three types of orbits: periodic orbits, which define fixed points in the Poincaré diagram; quasiperiodic orbits which define invariant curves surrounding the fixed points, and chaotic orbits which fill densely a part of the phase space. As described in [26], periodic orbits can be stable (elliptic), unstable (hyperbolic) and neutral (parabolic). To discern these properties for the elliptical stadium billiard, we use the criterion stated in [26], by which the stability of an orbit is assured if the absolute value of the trace of the deviation matrix M is smaller than 2, thus if

$$-2 < \mathrm{Tr}\, M < 2. \tag{6}$$

The deviation matrix of the closed orbit of period n can be written as $M = M_{12}M_{23}...M_{n1}$, where the 2×2 matrix M_{ik} for two subsequent impact points T_i and T_k, connected by a rectilinear path (the chord) of the length ρ_{ik}, is [26]

$$M_{ik} = \begin{pmatrix} -\dfrac{\sin\alpha_i}{\sin\alpha_k} + \dfrac{\rho_{ik}}{R_i\sin\alpha_k} & -\dfrac{\rho_{ik}}{\sin\alpha_i\sin\alpha_k} \\ -\dfrac{\rho_{ik}}{R_iR_k} + \dfrac{\sin\alpha_k}{R_i} + \dfrac{\sin\alpha_i}{R_k} & -\dfrac{\sin\alpha_k}{\sin\alpha_i} + \dfrac{\rho_{ik}}{R_k\sin\alpha_i} \end{pmatrix}. \tag{7}$$

To examine the properties of the elliptical stadium billiard in the full parameter space, one may proceed by scanning the complete array of δ and γ values. However, it is often sufficient to make use of a restricted, conveniently defined, one-parameter subspace. Depending on the property considered, we choose among the following possibilities: constant δ and changing γ, constant γ and changing δ as in [9], or $\delta = \gamma$ as in [8].

3.1. Billiards with $\delta < 1 - \gamma$

This subfamily of elliptical stadia has elongated semiellipses. The corresponding billiards have been investigated in [3–6], with the principal aim to establish the limiting shapes beyond which the billiard is fully chaotic. Parameters a and h used there to describe the boundary are connected with our parameters δ and γ through relations

$$\gamma = \frac{1}{h+a}, \quad \delta = \frac{h}{h+a}. \tag{8}$$

The results reported in [4,6] suggest that in the parameter space there exists a lower limit above which the billiard is chaotic, as a consequence of the existence of the stable pantographic orbits. In Fig. 3 results of our numerical calculations of the Poincaré sections are shown for $\delta = 0.19$ and different values of $\gamma < 1 - \delta$. This example conveniently illustrates the behavior typical for this region of the parameter space. Numerous elliptic islands arising from the stable pantographic orbits can be recognized. The islands due to some other types of orbits are also visible. Typical orbits contributing to these pictures are shown in Fig. 4, for $\delta = 0.19$ and increasing values of γ. The lowest two pantographic orbits, the bow-tie orbit ($n = 1$) and the candy orbit ($n = 2$), are shown in Figs. 4(f) and (h), respectively. Three higher period

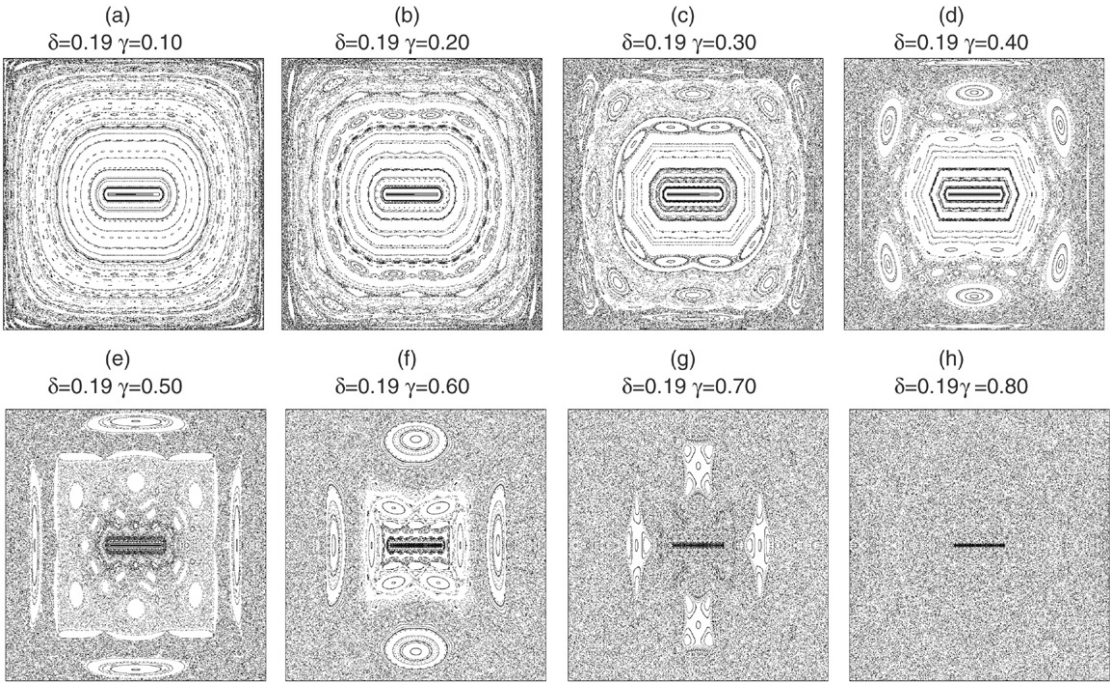

Fig. 3. Poincaré plots for $\delta < 1 - \gamma$, obtained by plotting the pairs of variables $-1 \leq X \leq 1$ and $-1 \leq V_x \leq 1$ for $\delta = 0.19$ and various values of γ.

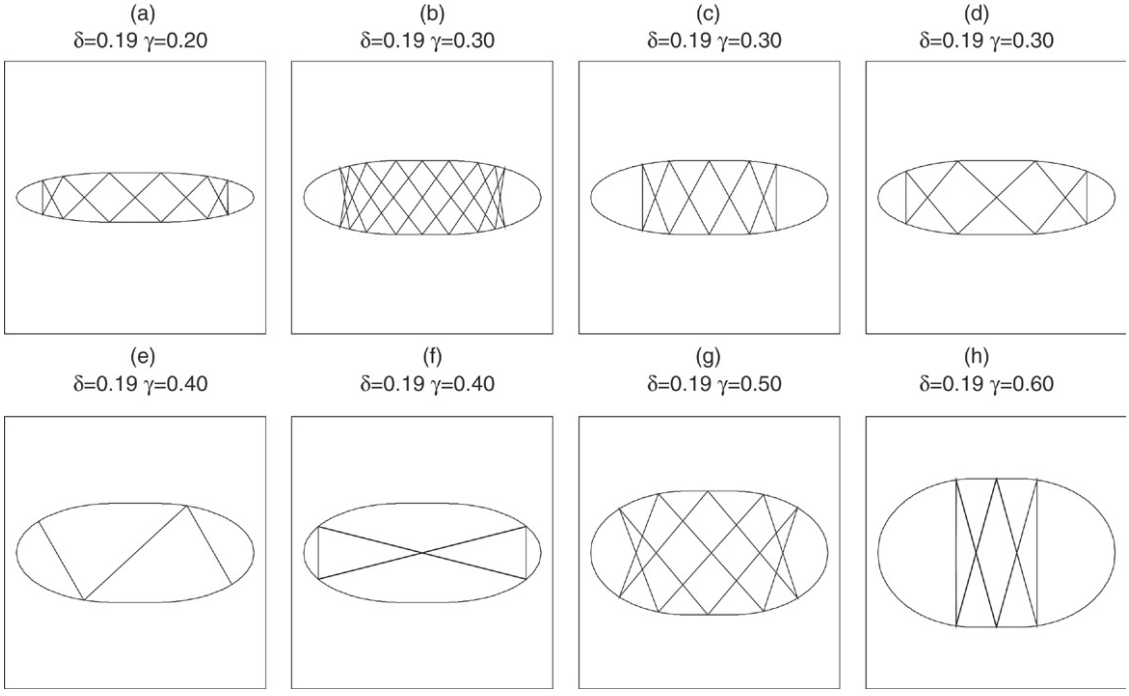

Fig. 4. Some typical orbits appearing for $\delta < 1 - \gamma$. Orbits in (a), (c), (d), (f) and (h) are pantographic orbits with $n = 4, 3, 2, 0$ and 1, respectively.

pantographic orbits are seen in Figs. 4(a), (c) and (d). Some other types of orbits are depicted in Figs. 4(b), (e) and (g).

In [5], an earlier conjecture of Donnay [3], stating that the lower limit of chaos is set by relations $1 < a < \sqrt{4 - 2\sqrt{2}}$ and $h > 2a^2\sqrt{a^2 - 1}$, was investigated. In our parametrization this region is delimited by functions

$$\gamma = \frac{1 - \delta}{\sqrt{4 - 2\sqrt{2}}}, \tag{9}$$

$$\gamma = \frac{\sqrt{2}(1 - \delta)^2}{\delta} \sqrt{\sqrt{1 + \left(\frac{\delta}{1 - \delta}\right)^2} - 1}, \tag{10}$$

$$\gamma = 1 - \delta. \tag{11}$$

In order to visualize the segmentation of the parameter space into regions of different dynamical behavior, in Fig. 5(a) we plot the pairs of shape parameters as points in the γ–δ diagram. Possible parameter choices are situated within an infinitely long

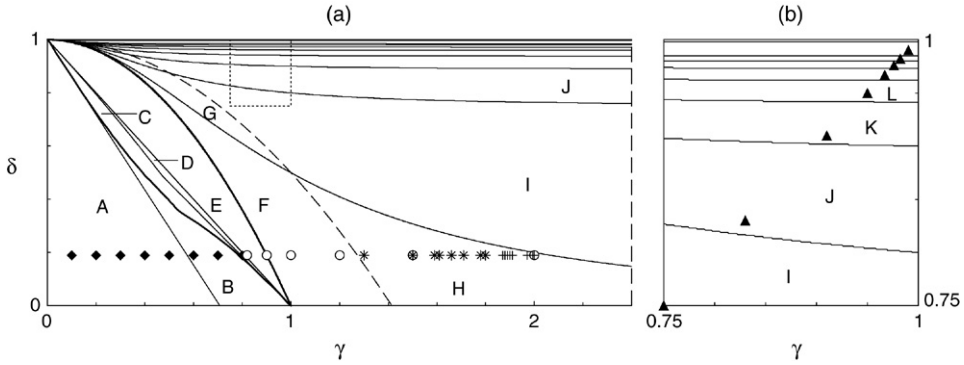

Fig. 5. (a) Diagram of the two-dimensional parameter space (γ, δ). Thick lines denote the border of the fully chaotic region including parts C, D and E. (b) Enlarged part of (a) showing the emergence of multidiamond orbits of higher n. Diamonds, circles, triangles, stars and crosses correspond to the cases illustrated on Figs. 3, 6 and 8–10, respectively.

horizontal band of height 1. The tilted line connecting the points (0, 1) and (1, 0) holds for Bunimovich stadia. The points below and above this line, respectively, are the elongated and the flattened elliptical stadia. The region delimited by functions (9)–(11) is visible as a narrow quasi-triangular area denoted by D in Fig. 5(a). The obtuse angle of this quasi-triangle is situated at the point $\gamma = 0.48711$, $\delta = 0.47276$. In a recent paper Del Magno and Markarian [7] proved exactly that for this region of the parameter space the elliptical stadium billiard is fully chaotic (ergodic with K- and Bernoulli properties). However, there are strong indications that the lowest limit of chaoticity is not consistent with this line. It can be probably identified with the limit derived in [4], separating regions B and C in Fig. 5(a) and resulting from the onset of the stable pantographic orbits. Whereas the lower limit of region D consists of two parts, this new limit is made of an infinite number of shorter segments, corresponding to all possible pantographic indices n [6]. Our numerical calculations based on the box-counting method (described in the next section) confirm the chaoticity of region C and identify the border between regions B and C in the parameter space as the lower limit of chaos.

Another conspicuous feature of billiards with $\delta < 1 - \gamma$ is the stickiness of certain orbits and consequent fragmentation of the chaotic part of the phase space into two or more separate sections. This occurs below a certain limiting combination of δ and γ. The exact shape of this limit is not obvious. It is probably connected with the straight line $\delta = 1 - \gamma\sqrt{2}$, pointed out in [3], separating in Fig. 5(a) region A from region B, which can be blamed on the discontinuities in the boundary curvature at the points where the flat parts join the elliptical arcs. Similar phenomena have been noticed in various billiards with circular arcs [27,28].

3.2. Billiards with $\delta > 1 - \gamma$

This part of the parameter space, comprising the flat half-ellipses, had not been investigated previously, except for the brief analysis in [2], later cited in [29]. As an example of the typical behavior, the Poincaré sections for $\delta = 0.19$ and various $\gamma > 1 - \delta$ are shown in Fig. 6. Here appear some new types of orbits and we examine their existence and stability. These are the diametral orbits (horizontal, vertical and tilted) of period two, the hour-glass orbit of period four, the diamond orbit of period four, as well as the whole family of multidiamond orbits. In our further description, we will refer to the impact coordinates x and y in the first quadrant (instead of $|x|$ and $|y|$), with no loss of generality for the obtained results, due to the symmetries of the boundary and of the considered orbits.

3.2.1. Diametral horizontal and vertical two-bounce orbits

The horizontal two-bounce orbit obviously exists for all combinations of δ and γ. However, the trace of the deviation matrix [26] is equal to

$$\mathrm{Tr}\, M = 2\left[2\left(\frac{\rho}{R} - 1\right)^2 - 1\right], \tag{12}$$

where $\rho = 2$ and $R = \gamma^2/(1-\delta)$, so that the stability condition (6) reads

$$\frac{\rho}{2R} < 1. \tag{13}$$

Hence the two-bounce horizontal diametral orbit becomes stable for

$$\delta > 1 - \gamma^2; \quad \gamma > \sqrt{1-\delta}. \tag{14}$$

Thus, there is a bifurcation at the value $\delta = 1 - \gamma^2$ giving birth to the stable diametral orbit. Again we choose $\delta = 0.19$ as a typical example, and keeping it constant we notice that for this value of δ the upper limit of chaos is $\gamma = \sqrt{1 - 0.19} = 0.9$. In the region $1 - \gamma < \delta < 1 - \gamma^2$, denoted in Fig. 5(a) by E, there are no periodic orbits, and this is the region of full chaoticity. This result has been proved in [2], among results for several chaotic billiards, and later cited in a discussion of the elliptical stadium billiards [29]. (It should be mentioned that for this case the definition of the shape parameter in [29] differs from that in Eq. (8).)

In the Poincaré plot, the invariant points of the horizontal diametral orbit are defined as $(0, \pm 1)$, since this orbit can be understood as a limiting case of a long and thin horizontal hour-glass orbit, which will be discussed below in more detail. The Poincaré diagrams in Fig. 6 show that the corresponding elliptic island arising for higher values of γ above the $\gamma = \sqrt{1-\delta}$ line develops into a broad band filled with invariant curves. The corresponding orbit will be shown below in Fig. 11(a).

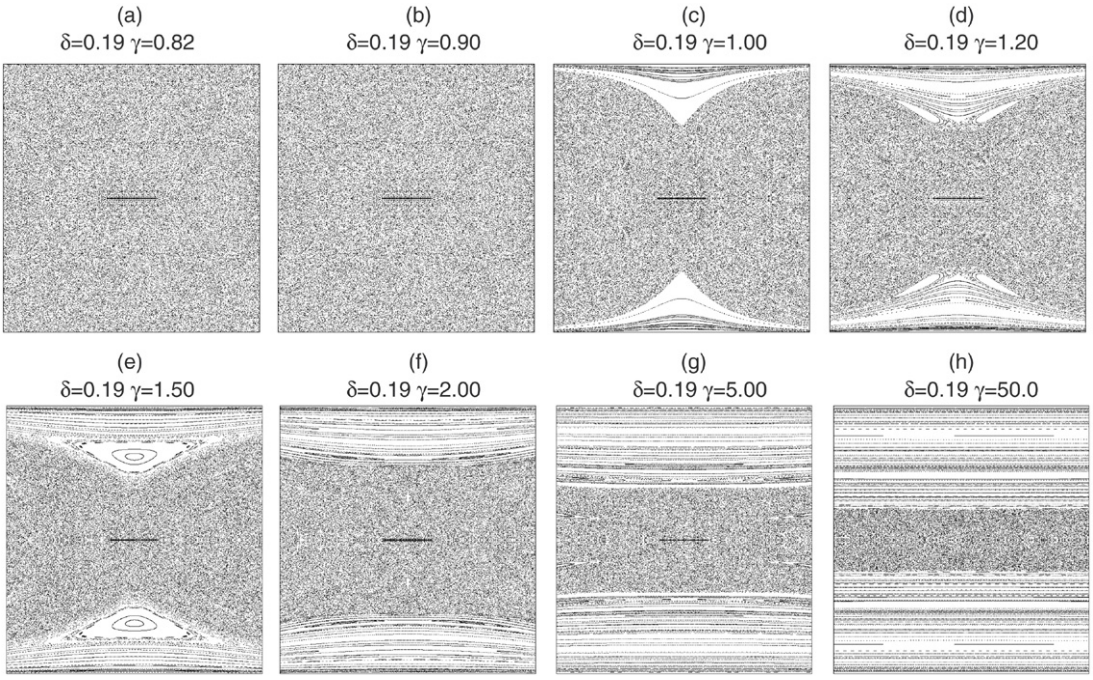

Fig. 6. Poincaré plots for $\delta = 0.19$ and various γ, for $\gamma > 1 - \delta$.

Here we mention also the existence of a family of the vertical two-bounce non-isolated neutral periodic orbits. Their properties are identical to those of the bouncing-ball orbits between the flat segments of the boundary in the Bunimovich stadium billiard [26] and at present do not require our further attention.

3.2.2. Tilted diametral two-bounce orbits

A tilted two-bounce orbit having the impact point $\mathrm{T}(x, y)$ on the billiard boundary with derivative y' exists if the following condition is fulfilled:

$$yy' + x = 0. \tag{15}$$

This is satisfied if

$$x = \frac{\gamma^2\delta}{\gamma^2 - (1-\delta)^2}. \tag{16}$$

This point should be on the elliptical part of the boundary $\delta < x < 1$, which leads to the condition

$$\gamma > \sqrt{1-\delta}. \tag{17}$$

However, from the stability condition (13), where the chord length is

$$\rho = 2\gamma\sqrt{1 + \frac{\delta^2}{\gamma^2 - (1-\delta)^2}}, \tag{18}$$

arises the restriction

$$\gamma < \sqrt{1-\delta}, \tag{19}$$

which cannot be fulfilled simultaneously with Eq. (17). The conclusion is that no stable tilted two-bounce orbit can exist.

3.2.3. Diamond orbit

The diamond orbit of period four shown in Fig. 7(a) exists for any parameter choice. It has two bouncing points at the ends of the horizontal semiaxis, and the other two on the flat parts on the boundary. To assess its stability, one should calculate the deviation matrix $M = (M_{01}M_{10})^2$. The angles contained in the matrix are given as $\sin\alpha_0 = \gamma/\rho$ and $\sin\alpha_1 = 1/\rho$, where $\rho = \sqrt{1+\gamma^2}$. The curvature radius at the point $x = 1$ is $R = \gamma^2/(1-\delta)$. This leads to the trace of the matrix

$$\mathrm{Tr}\, M = 2\left[2\left(\frac{2\rho^2}{R} - 1\right)^2 - 1\right] \tag{20}$$

and to the condition $\rho^2 < R$ or $1 + \gamma^2 < \gamma^2/(1-\delta)$, thus the diamond orbit becomes stable when

$$\delta > \frac{1}{1+\gamma^2}; \quad \gamma > \sqrt{\frac{1}{\delta} - 1}. \tag{21}$$

This limiting curve is shown in Fig. 5(a) as a full line dividing region F from G and region H from I.

3.2.4. Multidiamond orbits

The multidiamond orbit of order n is the orbit of period $2 + 2n$, which has two bouncing points at the ends of the horizontal axis and $2n$ bouncing points on the flat parts of the boundary (Fig. 7). Such an orbit exists if

$$\delta > 1 - \frac{1}{n}. \tag{22}$$

Thanks to the trick known from geometrical optics [10] which allows the mirroring of the billiard around the flat part of the boundary, the calculation of the deviation matrix for the order n becomes identical to the calculation of the matrix for

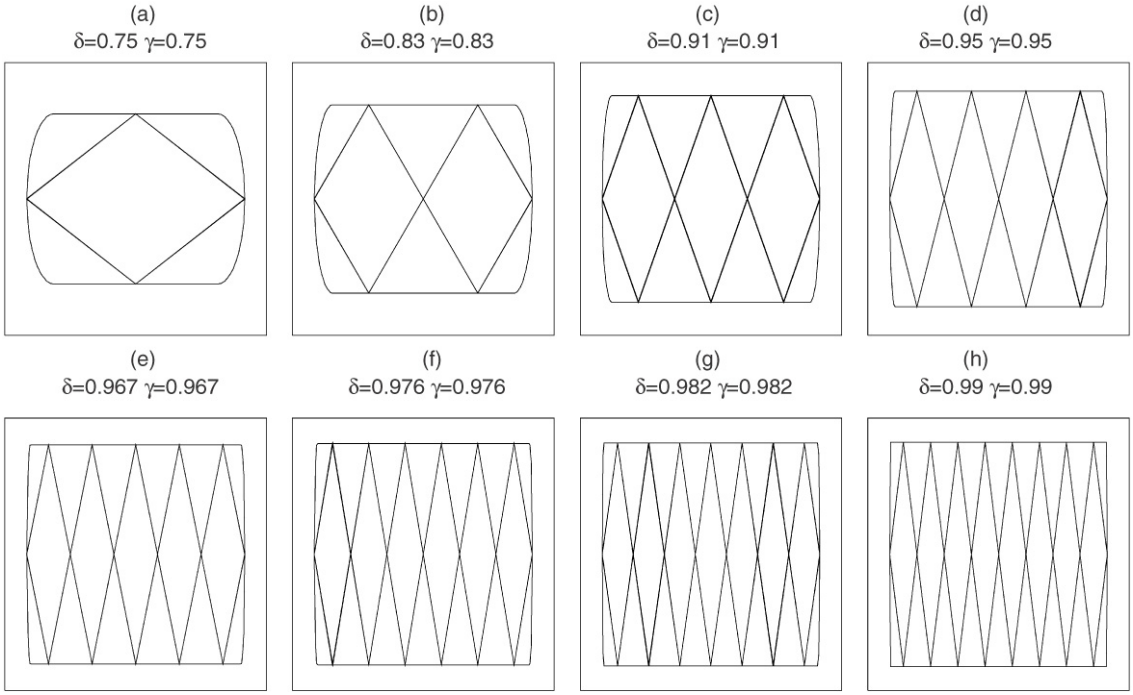

Fig. 7. Multidiamond orbits with $n = 1$–8.

the diamond orbit. Thus the chord length ρ in (20) should be replaced by

$$L = n\rho_n, \tag{23}$$

where

$$\rho_n = \sqrt{\frac{1}{n^2} + \gamma^2}. \tag{24}$$

The trace of the deviation matrix is then

$$\mathrm{Tr}\, M = 2\left[2\left(\frac{2\rho_n^2 n^2}{R} - 1\right)^2 - 1\right] \tag{25}$$

with $R = \gamma^2/(1-\delta)$. The resulting condition for the stability of the multidiamond orbit is then

$$\delta > 1 - \frac{\gamma^2}{1+\gamma^2 n^2}; \quad \gamma > \sqrt{\frac{1-\delta}{1-n^2(1-\delta)}}. \tag{26}$$

We stress again that the special case $n = 1$ corresponds to the diamond orbit. The limiting curves (26) are plotted in Fig. 5(a) and are shown enlarged in Fig. 5(b). For $\gamma \to \infty$ the minimal values of δ after which the multidiamond orbits appear are

$$\lim_{\gamma\to\infty} \delta = 1 - \frac{1}{n^2}. \tag{27}$$

The emergence of the stable multidiamond orbits can be followed by observing the Poincaré sections for a set of values $\delta = \gamma$ (Fig. 8). The values of δ for which an orbit of new n appears are given as intersections of the straight line $\delta = \gamma$ with curves defined by (26), and satisfy the equation

$$n^2\delta^3 - (n^2-1)\delta^2 + \delta - 1 = 0. \tag{28}$$

Especially, for the diamond orbit ($n = 1$) this equation reads

$$\delta^3 + \delta - 1 = 0 \tag{29}$$

and the orbit becomes stable for $\delta = \gamma = (u - 1/u)/\sqrt{3} = 0.6823278$, where $2u^3 = \sqrt{31} + \sqrt{27}$. For the same type of boundary the stable two-bounce orbit appeared at $\delta = \gamma = (\sqrt{5}-1)/2 = 0.618034$.

3.2.5. The hour-glass orbit

The hour-glass orbit looks like the bow-tie orbit rotated by $\pi/2$. It exists if the coordinates x and y of the impact point on the boundary and the derivative y' of the boundary at this point satisfy the equation

$$2xy' + yy'^2 - y = 0, \tag{30}$$

giving as solution the x-coordinate of the point of impact

$$x = \delta + \frac{(1-\delta)^2}{\gamma^2 - (1-\delta)^2}\left(\delta + \sqrt{\delta^2 + [\gamma^2 - (1-\delta)^2]}\right). \tag{31}$$

The condition $\delta < x < 1$ that this point should lie on the elliptical part of the boundary leads to the requirement

$$\delta > 1 - \frac{\gamma^2}{2}; \quad \gamma > \sqrt{2(1-\delta)}. \tag{32}$$

This limit is shown in Fig. 5(a) as a dashed line separating region G from I and region F from H. If we denote the points with positive y by 1 and the points on the negative side by -1, the deviation matrix can be calculated as

$$M = (M_{11}M_{1-1})^2 \tag{33}$$

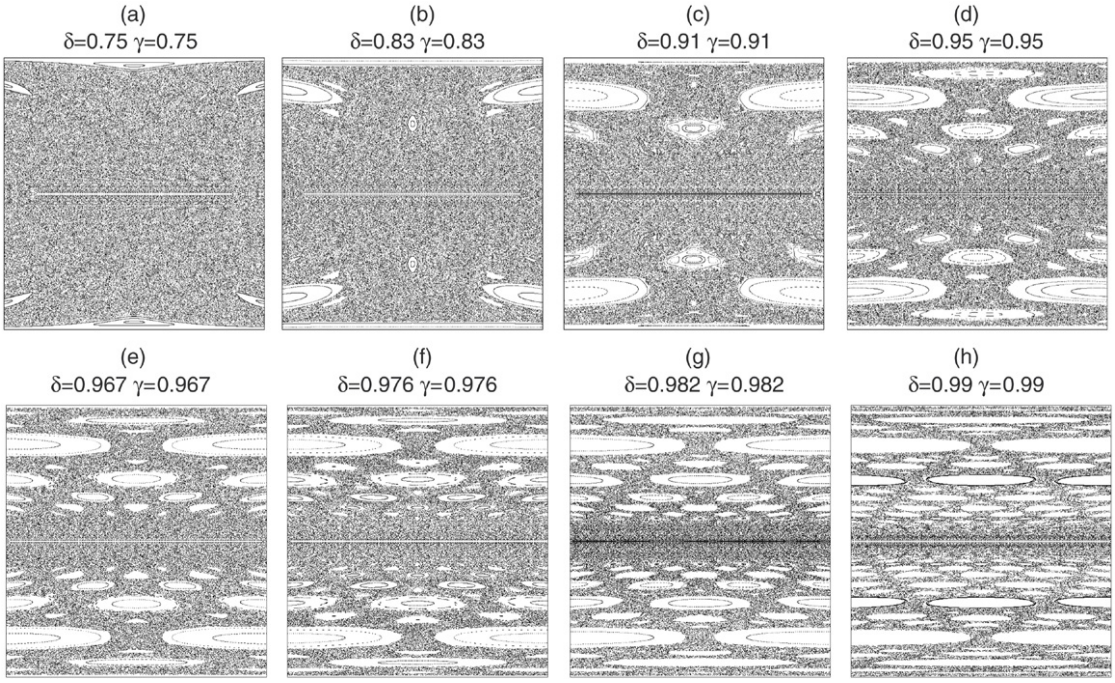

Fig. 8. Poincaré plots for a set of different values $\delta = \gamma$, showing the appearance of successive stable multidiamond orbits of higher order.

with x given by Eq. (31). The corresponding angle α needed in the matrix (7) is given by

$$\sin\alpha = \frac{\gamma(x-\delta)}{\sqrt{(1-\delta)^4 + (x-\delta)^2[\gamma^2 - (1-\delta)^2]}}. \tag{34}$$

The chords lengths are

$$\rho = \rho_{1,1} = 2x \tag{35}$$

and

$$\rho' = \rho_{1,-1} = 2\sqrt{x^2+y^2}, \tag{36}$$

where x is given by (31) and y is calculated from (1). The curvature radius at this point is obtained by substituting (31) into (4). If we define

$$\Phi = \frac{\rho}{R\sin\alpha}\frac{\rho'}{R\sin\alpha} - \left(\frac{\rho}{R\sin\alpha} + \frac{\rho'}{R\sin\alpha}\right) \tag{37}$$

the trace of the deviation matrix is

$$\mathrm{Tr}\, M = 2\Big[2(2\Phi+1)^2 - 1\Big]. \tag{38}$$

Whereas the left hand side of the stability condition (6) is valid automatically, its right hand side is fulfilled only if

$$-1 < \Phi < 0. \tag{39}$$

The left hand side limit of (39) $\Phi = -1$ reduces to the existence condition (32) and denotes the case where the hour-glass orbit degenerates into the horizontal diametral orbit. The right hand side limit $\Phi = 0$ is identical to the condition

$$\frac{\rho}{R\sin\alpha}\frac{\rho'}{R\sin\alpha} = \frac{\rho}{R\sin\alpha} + \frac{\rho'}{R\sin\alpha}, \tag{40}$$

giving the prescription for the numerical evaluation of the limit beyond which the hour-glass orbit becomes unstable. This is illustrated on Figs. 9 and 10, where Poincaré sections are shown for typical examples with $\delta = 0.19$ and a set of boundary shapes between $\gamma = \sqrt{2(1-\delta)} = 1.2728$ (where the stable orbit emerges) and $\gamma = 1.993$ (where it becomes hyperbolic). The island corresponding to the hour-glass orbit is shown enlarged, with different scales in Figs. 9 and 10. The evolution of the hour-glass orbit has very interesting properties. At first this island appears as a tiny point at the upper end of the Poincaré diagram, then descends following the value $V_x = \cos\phi$ of its vertical coordinate. When γ is varied, the central island acquires a resonant belt, with periodicity which changes from 8 to 7, then to 6, 5 and 4, as shown in Fig. 9. Near $\gamma = 1.79$ the orientation of the rectangular island changes from tilted to horizontal, after which a triangular island appears. Near $\gamma = 1.90$ (Fig. 10) the triangular island shrinks to infinitely small size, and then starts growing again, but with the opposite orientation. This is the phenomenon of the "blinking island" already noticed in [25] and described in [30]. With further increase of γ an interesting type of bifurcation takes place. The typical islands in the Poincaré sections corresponding to these changes are visible in Fig. 10, and the orbits in Fig. 11. At the value $\gamma = 1.993$, consistent with the upper stability limit expressed by (40), the stable hour-glass orbit in Fig. 11(e) is replaced by an unstable hour-glass orbit, shown in Fig. 11(f) for $\gamma = 2.02$. Simultaneously with this, two stable orbits appear. They have lost the symmetry of the hour-glass orbit, but in the mutual relation to each other, retain the left–right mirroring symmetry (Figs. 11(g) and (h)). This type of behavior, known as the pitchfork bifurcation, has been encountered in limaçon billiards [31].

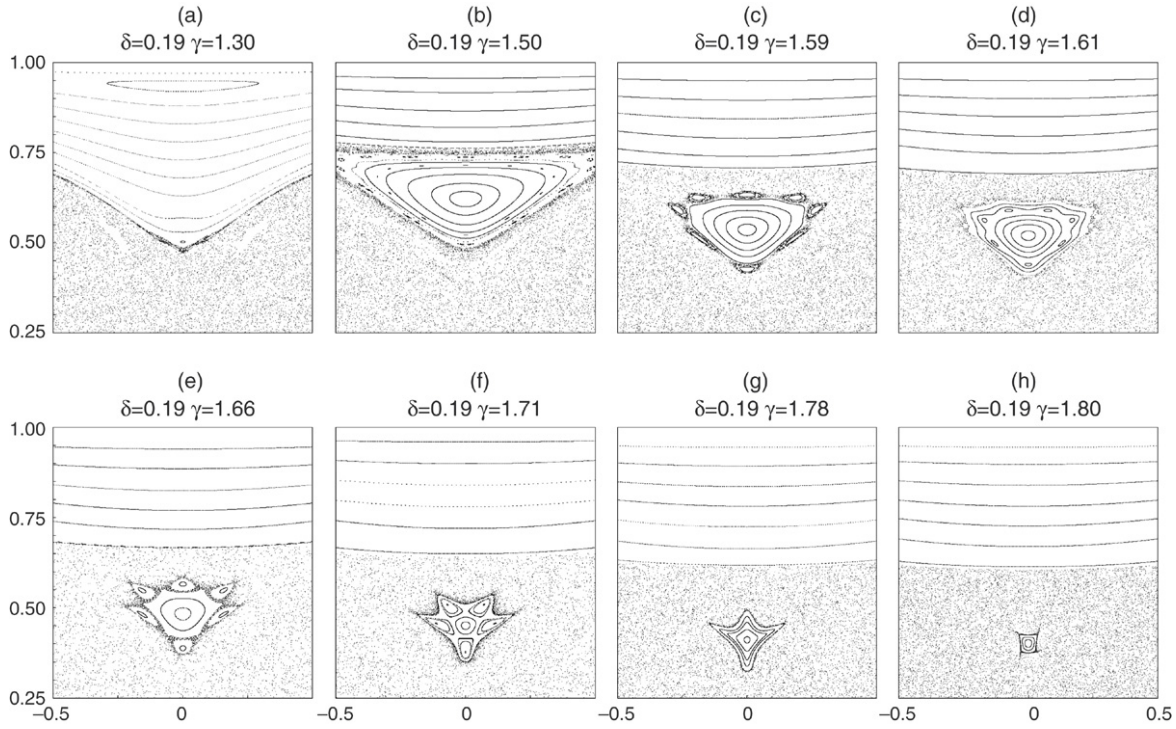

Fig. 9. Enlarged parts of the Poincaré plots, showing the stable island due to the hour-glass orbit, for $\delta = 0.19$ and $1.30 < \gamma < 1.80$.

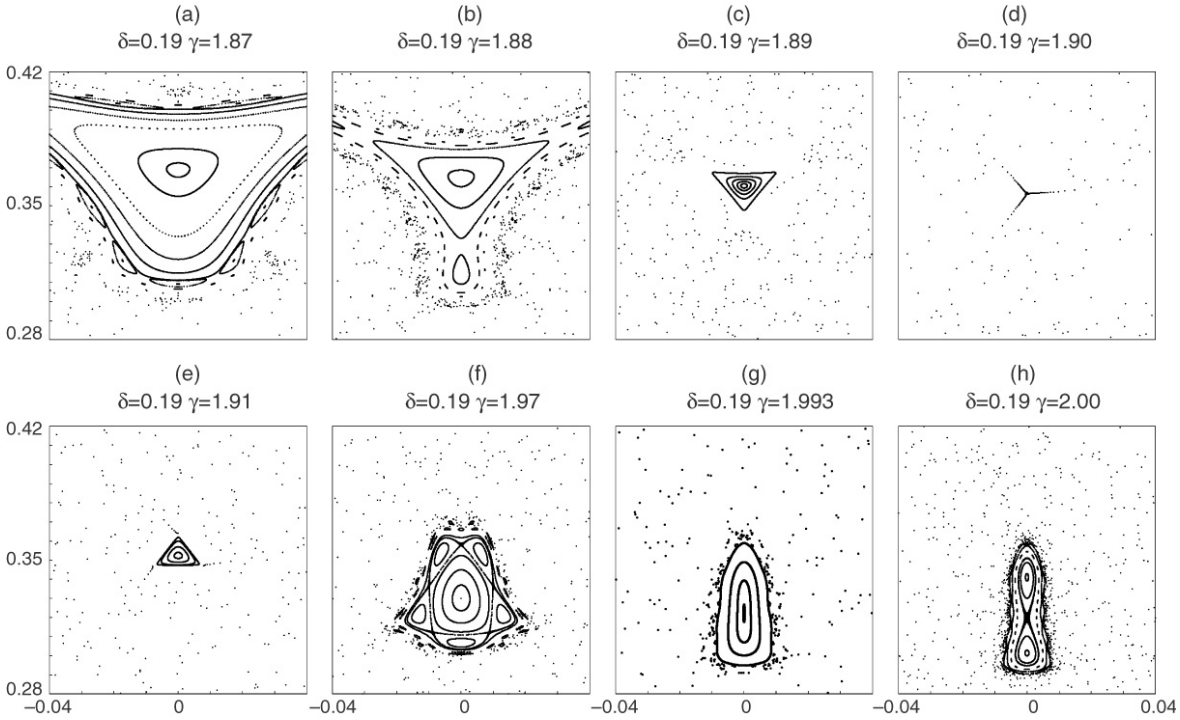

Fig. 10. Highly enlarged parts of the Poincaré plots, showing the stable island due to the hour-glass orbit, for $\delta = 0.19$ and $1.87 < \gamma < 2.00$.

4. Analysis of the parameter space properties by means of the box counting method

In this section we return to the question of limits within which the elliptical stadium billiard is fully chaotic. For $\delta > 1 - \gamma$, our numerical calculations of the billiard dynamics confirmed the result of [2,29], stating that the billiard is chaotic for $1-\gamma < \delta < 1-\gamma^2$. For $\delta < 1-\gamma$, it was proved in [7] that the billiard is fully chaotic for the narrow region determined by (9)–(11) below the Bunimovich line $\delta = 1 - \gamma$. In [4,6] this band was conjectured to be much broader, and its lower limit attributed to the emergence of the stable pantographic orbits.

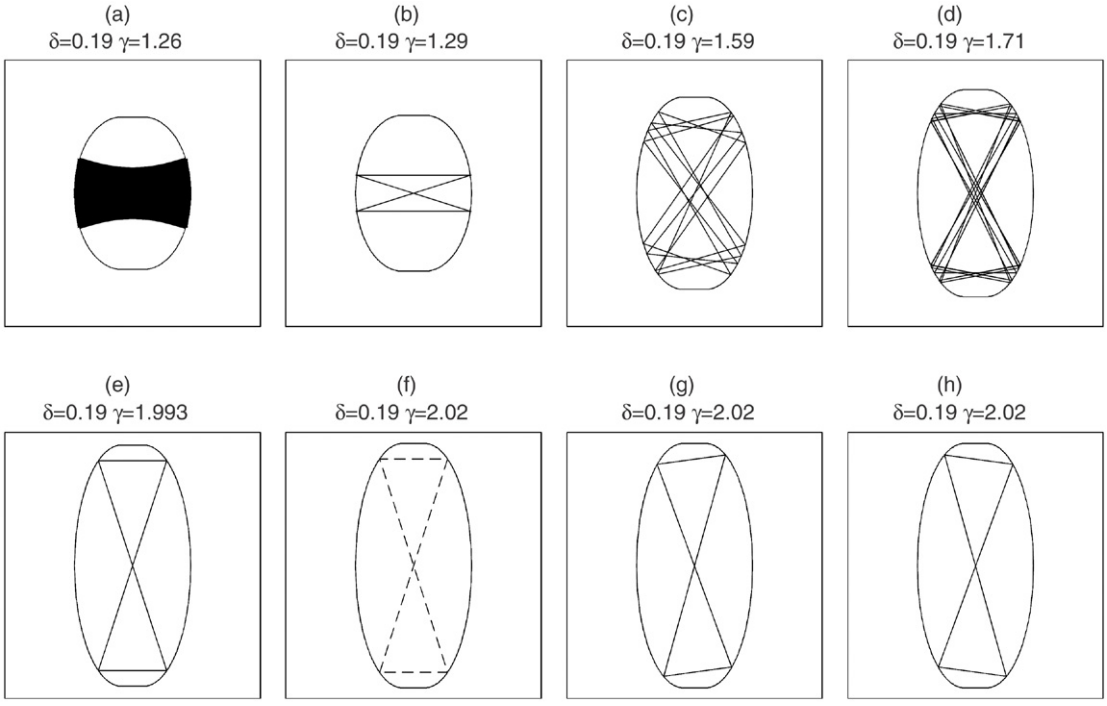

Fig. 11. (a) Stable orbit into which degenerate both the two-bounce horizontal orbit and the hour-glass orbit; (b) the hour-glass orbit near the lower limit of stability; (c), (d) orbits due to the resonant belts shown in Fig. 9; (e) stable hour-glass orbit at the upper stability limit; (f) unstable hour-glass orbit beyond the upper stability limit; (g), (h) two slightly deformed mutually symmetrical orbits, formed in the bifurcation of the hour-glass orbit.

Here we propose to test these limits numerically, by means of the box-counting method. We calculate the Poincaré sections for a chosen pair of shape parameters, starting with 5000 randomly chosen sets of initial conditions and iterating each orbit for 100 intersections with the x-axis, thus obtaining 500000 points (X, V_x) in the Poincaré diagram. Having in mind the symmetry of the billiard, we plot the absolute values $(|X|, |V_x|)$ of the computed pairs. Then we divide the obtained diagram into a grid of small squares of side 0.01, count the number n of squares which have points in them and calculate the ratio of this number to the total number N of squares. The obtained ratio n/N is denoted by q_{class} and determines the fraction of the chaotic region in the Poincaré section. In this way also certain points belonging to invariant curves within the regular islands are included. However, their contribution is negligible in comparison with the considerably larger chaotic contribution, since the average number of points per square is 50 and our principal aim is to examine the onset of complete chaos. Numerically, the size of the box has been varied until the saturation of n/N ratio was achieved, providing a consistent and reliable method of analysis of the set obtained in the numerical experiment. We proceed by calculating the chaotic fraction for a constant value of δ and varying γ. Results are shown in Fig. 12, where the classical chaotic fraction q_{class} is plotted against γ for a set of values of δ. These pictures show that for each δ there exist pronounced lower and upper limits of the fully chaotic region, characterized by $q_{\text{class}} = 1$. When one plots these limits in the parameter space diagram in Fig. 5(a), one obtains two curves, the upper one within the region $\delta > 1 - \gamma$, which coincides with Eq. (14) and separates region E from region F, and the lower one in the region $\delta < 1 - \gamma$, separating regions B and C. Thus our numerical experiments confirmed the existence of both limits, the lower one determined in [4] from the pantographic orbits, and the upper one suggested in [2]. Outside this fully chaotic region (consisting of regions C, D and E in Fig. 5(a)), the value of the fraction q_{class} is characterized by oscillations following the parameter variation, called in [27] the "breathing chaos". At some values there are strong discontinuities, which can be traced to bifurcations of various orbits.

5. The quantum-mechanical elliptical stadium billiard

The elliptical stadium billiard can also be considered as a two-dimensional quantal system. The Schrödinger equation for a particle of mass m moving freely within the two-dimensional billiard boundary is identical to the Helmholtz equation for the wave function Ψ

$$-\frac{\hbar^2}{2m}\nabla^2\Psi = E\Psi, \tag{41}$$

where E is the particle energy. The usual transformation to dimensionless variables is equivalent to substituting

$$\frac{\hbar^2}{2m} = 1 \quad \text{and} \quad E = k^2, \tag{42}$$

which yields

$$\left[\frac{\partial^2}{\partial x^2} + \frac{\partial^2}{\partial y^2} + k^2\right]\Psi(x, y) = 0. \tag{43}$$

We solve this equation following the method of Ridell [32] and, using the expansion in the spherical Bessel functions [33],

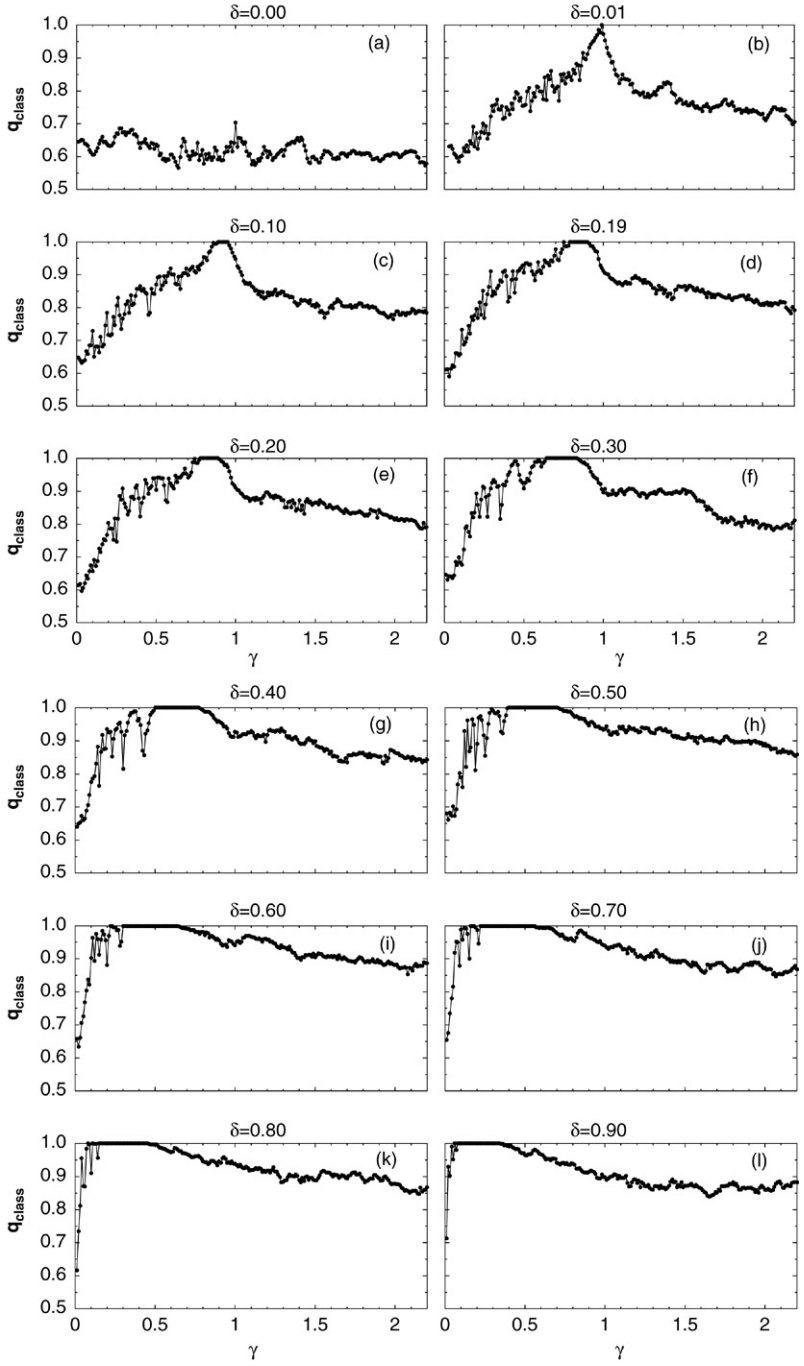

Fig. 12. Dependence of q_{class} on the shape parameter γ for various values of δ, calculated by means of the box-counting method. There is a conspicuous difference between the cases $\delta = 0$ and $\delta = 0.01$, typical for stadium billiards. For each $\delta \neq 0$ there exists an interval of full chaos, where $q_{\text{class}} = 1$.

obtain the wave functions and energy levels within the preselected energy interval. The described method yields about 500–3000 levels, depending on the shape.

5.1. Energy level statistics for the elliptical stadium billiard

According to [34,35], statistical properties of the energy spectrum reflect the degree of chaoticity in the corresponding classical system. For the elliptical stadium billiard it would be interesting to see whether the quantal calculation confirms the existence of the region of fully developed chaos, in the sense of the conjecture of Bohigas, Giannoni and Schmit [34]. To assess this correspondence, we calculate the spectrum and wave functions for a given pair of shape parameters. The obtained spectrum is then unfolded using the method of French and Wong [36] and the resulting histograms are analyzed by means of the Nearest Neighbor Spacing Distribution Method (NNSD). To fit the numerically calculated distributions, we propose three possibilities: the Brody distribution [37], the Berry–Robnik distribution [38], and a two-parameter generalization of both

Brody and Berry–Robnik distributions

$$P^{\mathrm{PR}}(s) = \mathrm{e}^{-(1-q)s}(1-q)^2 Q\left[\frac{1}{\omega+1}, \alpha q^{\omega+1} s^{\omega+1}\right] + \mathrm{e}^{-(1-q)s} q\left[2(1-q) + \alpha(\omega+1) q^{\omega+1} s^{\omega}\right] \mathrm{e}^{-\alpha q^{\omega+1} s^{\omega+1}} \quad (44)$$

which we shall henceforth call the Prosen–Robnik (PR) distribution. For $\omega = 1$, $P^{\mathrm{PR}}(s)$ reduces to the Berry–Robnik distribution, and for $q = 1$ it is identical to the Brody distribution. It coincides with the Wigner distribution if $\omega = 1$ and $q = 1$, and with the Poisson distribution whenever $\omega = 0$. Here, α is defined as

$$\alpha = \left[\Gamma\left(\frac{\omega+2}{\omega+1}\right)\right]^{\omega+1} \quad (45)$$

and Q denotes the Incomplete Gamma Function

$$Q(a,x) = \frac{1}{\Gamma(a)} \int_x^{\infty} \mathrm{e}^{-t} t^{a-1} \mathrm{d}t. \quad (46)$$

The derivation of Eq. (44) was based on the factorized gap distribution $Z^{\mathrm{PR}}(s)$

$$Z^{\mathrm{PR}}(s) = \mathrm{e}^{-(1-q)s} Q\left[\frac{1}{\omega+1}, \alpha q^{\omega+1} s^{\omega+1}\right] \quad (47)$$

introduced by Prosen and Robnik [39]. The gap distribution is the probability that no level spacing is present in the interval between s and $s + \Delta s$. The relation between the level spacing distribution $P(s)$ and the gap distribution is $P(s) = \mathrm{d}^2 Z(s)/\mathrm{d}s^2$. The function (44) has been evaluated in [40] and was used to test the spectra of several types of billiards of mixed type [25, 33]. Fitting the calculated histograms to this distribution gives two parameters q_{PR} and ω_{PR}. According to [39], the resulting value of q_{PR} is the variable which corresponds to the classical q_{class}, the magnitude of the chaotic fraction of the phase space. This distribution gives more realistic results than the Brody or the Berry–Robnik distribution.

The Berry–Robnik and Brody distributions have different behavior for very small spacings: the Brody distribution vanishes at $s = 0$, whereas for the Berry–Robnik distribution $P^{\mathrm{BR}}(0) = 1 - q^2$. Besides, the Berry–Robnik parameter q has a well defined physical meaning: quantitatively it is the fraction of the phase space which is filled with chaotic trajectories, whereas the remaining regular fraction of the phase space is equal to $1 - q$. However, the Berry–Robnik distribution is exactly applicable only in the semiclassical limit, and we are exploring the complete spectrum, including the lowest lying levels.

In [39] Prosen and Robnik argue that the distribution (44) describes simultaneously transition from semiclassical to quantal regime and transition from integrability to chaos. The two parameters ω and q characterize these two transitions, respectively, so that q retains its meaning as the chaotic fraction of the phase space, but is applicable also to cases far from the semiclassical limit. The diagram of (44) in dependence on ω and q has been presented in [40].

In applying the generalized distribution (44) to the billiard (1) we hold both parameters ω and q within the limits [0, 1]. We choose the subset of elliptical stadium billiards with $\delta = \gamma$, and in Figs. 13(a)–(k) we show the histograms and their fit with P^{PR}. In the region where $\delta = \gamma$ lies between 0.44 and 0.63 the distribution is very close to Wigner and $q_{\mathrm{PR}} = 1$. According to [34] this would correspond to complete classical chaos. In Fig. 13(l) some obtained values of q_{PR} are shown in dependence on δ and compared with the classical result obtained with the box-counting method. The values obtained with the Brody and Berry–Robnik distributions are also shown.

To the question whether the fluctuations of q_{class} with gradual changes in shape parameter reflect on the quantal values of q outside the chaotic region, the answer is positive, but requires further investigation. Considering the importance of bifurcations examined in Section 3, one can expect the effects similar to those found in the oval billiard [41].

6. Discussion and conclusions

In this work we have explored classical and quantal dynamics of the elliptical stadium billiards in the full two-parameter space, analyzing two distinct groups of these billiards, separated from each other by the set of Bunimovich billiards. For $\delta < 1 - \gamma$ we have confirmed the important role of the pantographic orbits in establishing the lower bound for chaos. For $\delta > 1 - \gamma$ we have analyzed in detail the diametral two-bounce orbits and the diamond and multidiamond orbits of increasing periodicity, creating numerous new corresponding elliptic islands when the value $\delta = 1$ is approached. Especially interesting is the behavior of the hour-glass orbit which is, while remaining stable within a large range of increasing values of γ, accompanied with a resonant belt with changing periodicity. At the value where the orbit becomes unstable, a bifurcation to a pair of stable quasi-hour-glass orbits with distorted symmetry appears. The upper limit of chaos $\delta = 1 - \gamma^2$ is obtained by estimating the stability of the horizontal two-bounce orbit, and coincides with the limit proposed in [2]. We have thus numerically confirmed the existence of a broad region of chaos in the parameter space surrounding the straight line belonging to the Bunimovich stadia.

Thus the most important dynamical phenomena of the elliptical stadium billiards in the full parameter space are revealed. There remains, however, the open question of the stickiness of orbits in the region $\delta < 1 - \gamma$, the fragmentation of the phase space and its connection with the discontinuities of the boundary curvature, and possible importance of the limiting straight line $\delta = 1 - \gamma\sqrt{2}$. One possible method to resolve this is to analyze the statistics and the phase space properties of the leaking billiards [42,43]. Preliminary investigations show promising results, and should be able to explain the foliation and the fragmentation of the phase space of the elliptical stadium billiard.

In conclusion, our investigation has revealed dynamical properties of a large two-parameter family of stadium-like billiards exhibiting a rich variety of integrable, mixed and chaotic behavior, in dependence on two shape parameters δ and γ, with the special case of $\delta = 1 - \gamma$ corresponding to the Bunimovich stadium billiard [1]. The proposed billiard

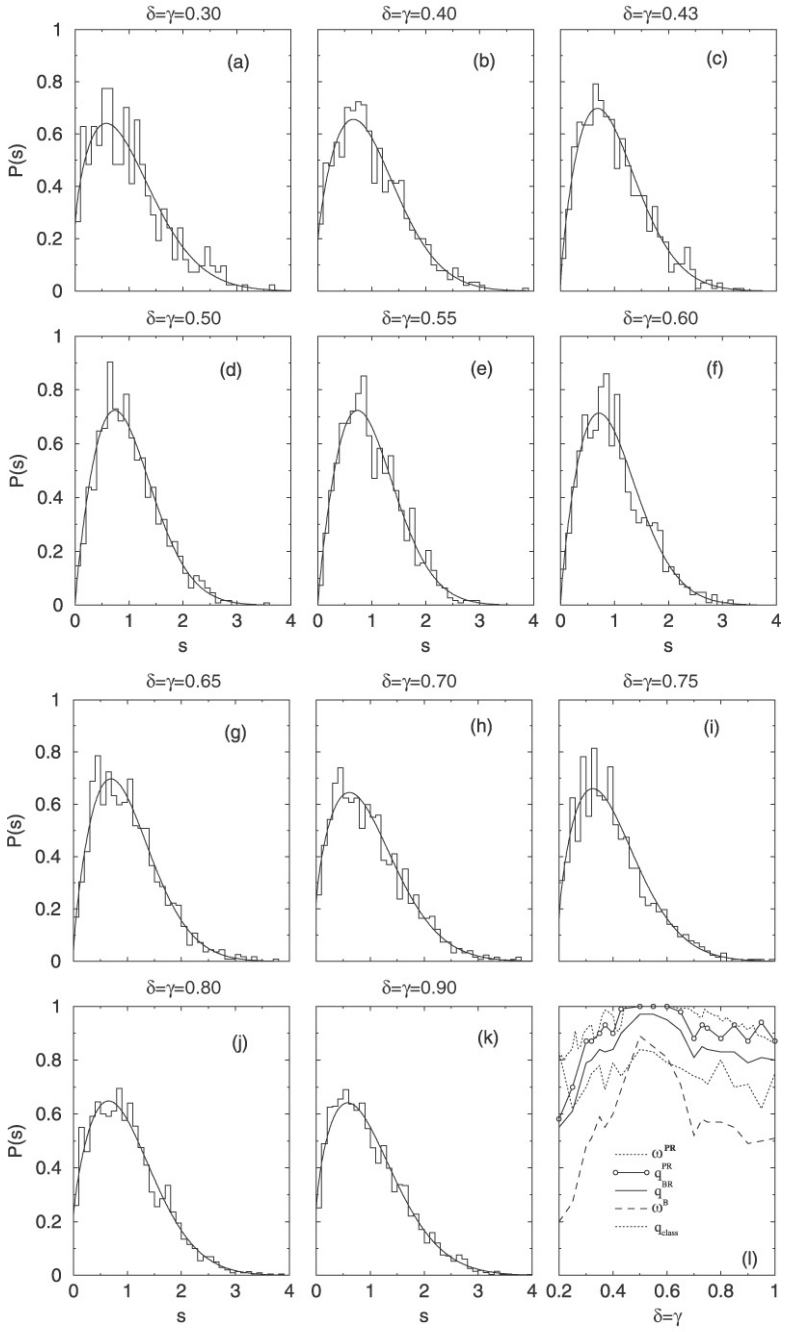

Fig. 13. (a)–(k) Histograms of the level density fluctuations for spectra of billiards with $\delta = \gamma$, fitted to the Prosen–Robnik distribution (44); (l) comparison of the classical chaotic fraction q_{class} with the values obtained by fitting the histograms with the Prosen–Robnik, Berry–Robnik and Brody distributions.

shapes and obtained results could serve as an additional testing ground for the experimental properties of semiconducting optical devices and microwave resonant cavities.

Acknowledgments

We are grateful to A. Bäcker, V. Dananić, M. Hentschel, T. Prosen and M. Robnik for enlightening discussions.

References

[1] L. Bunimovich, Funct. Anal. Appl. 8 (1974) 254.
[2] M. Wojtkowski, Commun. Math. Phys. 105 (1986) 391.
[3] V.J. Donnay, Commun. Math. Phys. 141 (1991) 225.
[4] E. Canale, R. Markarian, S. Oliffson Kamphorst, S. Pinto de Carvalho, Physica D 115 (1998) 189.
[5] R. Markarian, S. Oliffson Kamphorst, S. Pinto de Carvalho, Commun. Math. Phys. 174 (1996) 661.
[6] S. Oliffson Kamphorst, S. Pinto de Carvalho, Discr. Contin. Dyn. Syst. 7 (2001) 663.
[7] G. DelMagno, R. Markarian, Commun. Math. Phys. 233 (2003) 211.
[8] V. Lopac, I. Mrkonjić, D. Radić, Phys. Rev. E 66 (2002) 035202.
[9] V. Lopac, I. Movre, I. Mrkonjić, D. Radić, Progr. Theoret. Phys. Suppl. 150 (2003) 371.
[10] L.A. Bunimovich, Chaos 11 (2001) 802.
[11] S. Lansel, M.A. Porter, L.A. Bunimovich, Chaos 16 (2006) 013129.

[12] C. Gmachl, F. Capasso, J.U. Nöckels, A.D. Stone, D.L. Sivco, A.Y. Cho, Science 280 (1998) 1556.
[13] M. Hentschel, K. Richter, Phys. Rev. E 66 (2002) 056297.
[14] C.W.J. Beenakker, Rev. Modern Phys. 69 (1997) 731.
[15] C.M. Marcus et al., Phys. Rev. Lett. 69 (1992) 506.
[16] V. Milner, J.L. Hanssen, W.C. Campbell, M.G. Raizen, Phys. Rev. Lett. 86 (2001) 1514.
[17] N. Friedman, A. Kaplan, D. Carasso, N. Davidson, Phys. Rev. Lett. 86 (2001) 1518.
[18] A. Kaplan, N. Friedmann, M. Andersen, N. Davidson, Phys. Rev. Lett. 87 (2001) 274101.
[19] L.A. Bunimovich, Regul. Chaotic Dynamics 8 (2003) 15; Nonimaging Optics: Maximum Efficiency Light Transfer VI, Proc. SPIE 4446-21, R. Winston Ed., Chicago 2001.
[20] J.A. Méndez-Bermúdez, G.A. Luna-Acosta, P. Seba, K.N. Pichugin, Phys. Rev. B 67 (2003) 161104R.
[21] Y.-H. Kim, M. Barth, H.-J. Stöckmann, J.P. Bird, Phys. Rev. B 68 (2003) 045315.
[22] E.G. Altmann, A.E. Motter, H. Kantz, Chaos 15 (2005) 033105.
[23] J. Stein, H.J. Stöckmann, Phys. Rev. Lett. 64 (1990) 2215.
[24] J. Stein, H.J. Stöckmann, U. Stoffregen, Phys. Rev. Lett. 75 (1995) 53.
[25] V. Lopac, I. Mrkonjić, D. Radić, Phys. Rev. E 64 (2001) 016214.
[26] M. Berry, European J. Phys. 2 (1981) 91.
[27] H.R. Dullin, P.H. Richter, A. Wittek, Chaos 6 (1996) 43.
[28] S. Ree, L.E. Reichl, Phys. Rev. E 60 (1999) 1607.
[29] R. Markarian, Nonlinearity 6 (1993) 819.
[30] G.M. Zaslavsky, M. Edelman, B.A. Nyazov, Chaos 7 (1996) 159.
[31] H.R. Dullin, A. Bäcker, Nonlinearity 14 (2001) 1673.
[32] R.J. Ridell Jr., J. Comput. Phys. 31 (1979) 21, 42.
[33] V. Lopac, I. Mrkonjić, D. Radić, Phys. Rev. E 59 (1999) 303.
[34] O. Bohigas, M.J. Giannoni, C. Schmit, Phys. Rev. Lett. 52 (1984) 1.
[35] G. Casati, F. Valz-Gris, I. Guarnero, Lett. Nuovo Cimento 28 (1980) 279.
[36] J.B. French, S.S.M. Wong, Phys. Lett. B 35 (1971) 5.
[37] T.A. Brody, Lett. Nuovo Cimento 7 (1973) 482.
[38] M.V. Berry, M. Robnik, J. Phys. A 17 (1984) 2413.
[39] T. Prosen, M. Robnik, J. Phys. A 26 (1993) 2371.
[40] V. Lopac, S. Brant, V. Paar, Z. Phys. A 356 (1996) 113.
[41] H. Makino, T. Harayama, Y. Aizawa, Phys. Rev. E 63 (2001) 056203.
[42] D.N. Armstead, B.R. Hunt, E. Ott, Physica D 193 (2004) 96.
[43] J. Schneider, T. Tél, Z. Neufeld, Phys. Rev. E 66 (2002) 066218.